






# Structural amyloid plaque polymorphism is associated with distinct lipid accumulations revealed by trapped ion mobility mass spectrometry imaging

Wojciech Michno<sup>1,2,3</sup>  | Patrick M. Wehrli<sup>1</sup> | Srinivas Koutarapu<sup>1</sup> | Christian Marsching<sup>4</sup> | Karolina Minta<sup>1</sup> | Junyue Ge<sup>1</sup> | Sven W. Meyer<sup>5</sup> | Henrik Zetterberg<sup>1,6,7,8</sup>  | Kaj Blennow<sup>1,6</sup> | Corinna Henkel<sup>5</sup> | Janina Oetjen<sup>5</sup>  | Carsten Hopf<sup>4</sup>  | Jörg Hanrieder<sup>1,6,7</sup> 

<sup>1</sup>Department of Psychiatry and Neurochemistry, Institute of Neuroscience and Physiology, Sahlgrenska Academy, University of Gothenburg, Mölndal, Sweden

<sup>2</sup>Department of Neuroscience, Physiology and Pharmacology, University College London, Gower Street, London, UK

<sup>3</sup>Department of Pediatrics, Stanford University School of Medicine, Stanford University, Stanford, California, USA

<sup>4</sup>Center for Mass Spectrometry and Optical Spectroscopy (CeMOS), Mannheim University of Applied Sciences, Mannheim, Germany

<sup>5</sup>Bruker Daltonics GmbH & Co. KG, Bremen, Germany

<sup>6</sup>Clinical Neurochemistry Laboratory, Sahlgrenska University Hospital Mölndal, Mölndal, Sweden

<sup>7</sup>Department of Neurodegenerative Disease, Queen Square Institute of Neurology, University College London, London, UK

<sup>8</sup>UK Dementia Research Institute, University College London, London, UK

## Correspondence

Wojciech Michno, Department of Pediatrics, Stanford University School of Medicine, Center for Clinical Sciences Research (CCSR), Stanford University, 269 Campus Drive, Stanford, CA 94305-5119, USA.

Email: [wmichno@stanford.edu](mailto:wmichno@stanford.edu)

Jörg Hanrieder, Department of Psychiatry and Neurochemistry, University of Gothenburg, Sahlgrenska University Hospital Mölndal, House V3, 43180 Mölndal, Sweden.

Email: [jh@gu.se](mailto:jh@gu.se)

## Funding information

Swedish Research Council VR, Grant/Award Number: 2018-02181, 2018-02532 and 2017-00915; Alzheimerfonden;

## Abstract

Understanding of Alzheimer's disease (AD) pathophysiology requires molecular assessment of how key pathological factors, specifically amyloid  $\beta$  (A $\beta$ ) plaques, influence the surrounding microenvironment. Here, neuronal lipids have been implicated in A $\beta$  plaque pathology, though the lipid microenvironment in direct proximity to A $\beta$  plaques is still not fully resolved. A further challenge is the microenvironmental molecular heterogeneity, across structurally polymorphic A $\beta$  features, such as diffuse, immature, and mature, fibrillary aggregates, whose resolution requires the integration of advanced, multimodal chemical imaging tools. Herein, we used matrix-assisted laser desorption/ionization trapped ion mobility spectrometry time-of-flight based mass spectrometry imaging (MALDI TIMS TOF MSI) in combination with hyperspectral confocal microscopy to probe the lipidomic microenvironment associated

**Abbreviations:** AD, Alzheimer's disease; A $\beta$ , amyloid- $\beta$ ; CCS, collisional cross-section; Cer, ceramide; CR, congo red; ESI, electrospray ionization; GL, glycerolipids; GM, mono sialated-gangliosides; GP, glycerophospholipids; LC, liquid chromatography; LCO, luminescent-conjugated oligothiophenes; LPA, lysophosphatidic acid; LPC, lysophosphatidylcholine; LPI, lysophosphoinositol; MALDI-MSI, matrix-assisted laser/desorption ionization-mass spectrometry imaging; OPLS-DA, orthogonal projection to latent structure-discriminant analysis; PA, phosphatidic acid; PC, phosphatidylcholine; PCA, principal component analysis; PE, phosphoethanolamine; PI, phosphoinositol; PS, phosphoserine; ROI, region of interest; SL, sterol lipids; SP, sphingolipids; ST, sulfatide; TIMS, trapped ion mobility spectrometry; TOF, time of flight.

Wojciech Michno and Patrick M. Wehrli contributed equally to this work.

A preprint of this article was posted on chemRxiv on October 19, 2021. <https://doi.org/10.33774/chemrxiv-2021-w1470>; <https://chemrxiv.org/engage/chemrxiv/article-details/616d32968b620d7399535eb6>.

This is an open access article under the terms of the Creative Commons Attribution License, which permits use, distribution and reproduction in any medium, provided the original work is properly cited.

© 2021 The Authors. *Journal of Neurochemistry* published by John Wiley & Sons Ltd on behalf of International Society for Neurochemistry

Alzheimer Research UK; Hj rnfonden; Knut and Alice Wallenberg Foundation; European Research Council, Grant/Award Number: 681712; Swedish State Support for Clinical Research, Grant/Award Number: ALFGBG-720931;  hl n-Stiftelsen; Rune och Ulla Aml vs Stiftelse; Stiftelsen Gamla Tj narinnor; Federal Ministry of Education and Research, Grant/Award Number: 13FH8102IA; Gun och Bertil Stohnes Stiftelse; Agneta Prytz-Folkes och G sta Folkes Stiftelse; Torsten S derberg Foundation; Wilhelm & Martina Lundgrens Vetenskapsfond; Demensfonden; Frimurarestiftelsen

with structural polymorphism of A $\beta$  plaques in transgenic Alzheimer's disease mice (tgAPP<sub>SWE</sub>). Using on tissue and ex situ validation, TIMS MS/MS facilitated unambiguous identification of isobaric lipid species that showed plaque pathology-associated localizations. Integrated multivariate imaging data analysis revealed multiple, A $\beta$  plaque-enriched lipid patterns for gangliosides (GM), phosphoinositols (PI), phosphoethanolamines (PE), and phosphatidic acids (PA). Conversely, sulfatides (ST), cardiolipins (CL), and polyunsaturated fatty acid (PUFA)-conjugated phosphoserines (PS), and PE were depleted at plaques. Hyperspectral amyloid imaging further delineated the unique distribution of PA and PE species to mature plaque core regions, while PI, LPI, GM2 and GM3 lipids localized to immature A $\beta$  aggregates present within the periphery of A $\beta$  plaques. Finally, we followed AD pathology-associated lipid changes over time, identifying plaque- growth and maturation to be characterized by peripheral accumulation of PI (18:0/22:6). Together, these data demonstrate the potential of multimodal imaging approaches to overcome limitations associated with conventional advanced MS imaging applications. This allowed for the differentiation of both distinct lipid components in a complex micro-environment as well as their correlation to disease-relevant amyloid plaque polymorphs.

#### KEYWORDS

Alzheimer's disease, beta-amyloid, lipids, luminescent-conjugated oligothiophenes, matrix-assisted laser/desorption ionization mass spectrometry imaging, trapped ion mobility spectrometry

## 1 | INTRODUCTION

With the average age of the World's population increasing, the prevalence of age-associated diseases including neurodegenerative disorders is increasing as well. Alzheimer's disease (AD) is the most common form of dementia and the most common neurodegenerative disease affecting 12% over 65. The major pathologic hallmark of AD includes the formation of extracellular plaques consisting of amyloid- $\beta$  (A $\beta$ ) peptides as well as neurofibrillary tangles formed by hyper-phosphorylated tau protein (Masters et al., 2015).

A $\beta$  pathology has been established to precede other downstream pathologic features, suggesting that amyloid peptide secretion and aggregation are key pathogenic events in AD pathogenesis. However, the exact chain of events underlying amyloid pathology and AD pathogenesis are still not fully understood hampering the development of any curative treatments with significant clinical and socioeconomic consequences (Masters et al., 2015; Scheltens et al., 2016).

A further challenge in understanding the biochemical basis underlying AD pathogenesis is the complex, phenotypic heterogeneity of AD pathology and A $\beta$  plaque morphology in particular. Polymorphic A $\beta$  pathology involves structurally different amyloid aggregates within and across different plaque phenotypes (Rasmussen et al., 2017). Most prominently, mature plaques associated with AD pathology are characterized by the formation of a compact core that

was found to consist mainly of A $\beta$  1-40 (Michno, Nystrom, et al., 2019). With background to the complexity of plaque pathology and the still limited knowledge thereof, it comes to no surprise that major pharmacotherapeutic strategies targeting A $\beta$  plaque pathology have not been successful so far.

This, in turn, highlights the immediate need to further elucidate the molecular architecture associated with plaque formation in AD. Indeed, key developments in bioanalytical techniques, including chemical imaging, have increased our understanding of the molecular basis of single A $\beta$  deposit formation at subcellular scales. Particularly, mass spectrometry imaging (MSI) has gained prominent relevance for studying biochemical traits of AD pathology warranted by the molecular specificity inherent to this technique (Enzlein et al., 2020; Hanrieder et al., 2013; Kaya, Brinet, Michno, Baskurt, et al., 2017; Kaya et al., 2018; Michno, Wehrli, et al., 2019; Michno et al., 2018). Here, matrix-assisted laser desorption ionization (MALDI)-based MSI has been demonstrated to be a valuable approach in retrieving novel chemical information on plaque pathology in both AD patient's brain and AD mouse models. This includes also molecular information on plaque-associated neuronal lipid dynamics, which is significant in that lipids have been implicated in AD pathology and more specific in A $\beta$  plaque formation mechanisms before (Di Paolo & Kim, 2011). This is corroborated by the fact that the  $\epsilon$ 4 allele of the apolipoprotein E encoding gene (APOE), a lipid transporter, is the most prominent genetic risk factor for developing sporadic AD (Liu

et al., 2013). Although the relevance of lipids in AD pathology has long been recognized, the means for elucidating lipid biochemistry comprehensively and chemically specific at single plaque scales have not been available. Here, MALDI-MSI along with complementary chemical amyloid staining to delineate and annotate plaque polymorphism, identified plaque morphology-associated sphingolipid (SP), phosphatidylcholine (PC), lysolipid (LPC/LPA), and phosphoinositol (PI), species (Kaya, Brinet, Michno, Baskurt, et al., 2017; Kaya, Brinet, Michno, Syvanen, et al., 2017; Kaya et al., 2018; Michno et al., 2018).

The capacity of MSI has been significantly expanded due to the introduction of ion mobility into the MS system allowing further separation of structurally similar and even isomeric compounds, which is of great relevance given the complexity among different lipid classes (Gillig et al., 2000; Jackson et al., 2005, 2007; McLean et al., 2007; Trim et al., 2008).

In this study, we set out to elucidate plaque morphology-associated lipid species in a transgenic AD mouse model (tgAPP<sub>SWE</sub>) that displays polymorphic plaque pathology (Philipson et al., 2010). We used a novel MALDI-MSI setup with trapped ion mobility spectrometry (TIMS) to further resolve plaque-associated lipid species. The MSI experiments were interfaced with fluorescent amyloid staining on the same section using structure sensitive, electrooptic amyloid probes, luminescent-conjugated oligothiophenes (LCOs) (Nilsson, 2009) that allow to delineate structurally different amyloid aggregates (Nilsson et al., 2007; Nystrom et al., 2013; Rasmussen et al., 2017). This hyperspectral imaging approach identified distinct lipid localization patterns specific to polymorphic amyloid structures including mass overlapping compounds, which could be further resolved by ion mobility separation.

## 2 | METHODS

### 2.1 | Chemicals and reagents

All chemicals for matrix and solvent preparation were pro-analysis grade and obtained from Sigma-Aldrich/Merck unless otherwise specified. TissueTek optimal cutting temperature compound was purchased from Sakura Finetek (Cat. no: 4583; AJ Alphen aan den Rijn). Deionized water obtained by a Milli-Q purification system (Millipore Corporation).

### 2.2 | Animals

Transgenic male tgAPP<sub>SWE</sub> mice, 18 and 23 months of age ( $n = 3$  per age group), carrying the Swedish (K670N, M671L) mutations of human APP were studied. The animals were reared ad libitum and housed in groups at an animal facility at Uppsala University, Sweden under a 12/12 light cycle. The animals were anesthetized with isoflurane and sacrificed by decapitation. The brains were dissected quickly within >3 min postmortem delay and frozen on dry ice. All animal procedures were approved by an ethical committee and performed in compliance

with national and local animal care and use guidelines (DNr #C17/14 at Uppsala University). For this study, no randomization, blinding, and sample size calculations were performed. All animal experiments and reporting were performed according to the ARRIVE guidelines. This exploratory study was not preregistered and not randomized. No inclusion or exclusion criteria were applied. No sample size calculation was performed, though post-hoc power calculations were included for validation (see 2.6 Data Analysis).

### 2.3 | Sample preparation

Tissue sections (12  $\mu\text{m}$ ) were collected on a cryostat microtome (Leica CM1900; Leica Biosystems) and thaw mounted onto indium tin oxide-coated, conductive glass slides (Cat. no: 237001; Bruker Daltonics GmbH & Co. KG) and stored at  $-80^\circ\text{C}$  until further use. For matrix deposition, samples were thawed in a desiccator under reduced pressure for 30 min. 2-(1-naphthylamino) ethylamine dihydrochloride (NEDC) (Cat. no.: 222488-5G; Sigma-Aldrich) was used as a matrix and applied to the tissue sections using a TM sprayer (HTX Technologies) equipped with a P-580 HPLC pump (Dionex). Before spraying, the solvent pump was purged with 70% acetonitrile (ACN, Cat. no.: 34851-1L; Sigma-Aldrich) at 500  $\mu\text{l}/\text{min}$  for 10 min followed by a manual rinse of matrix loading loop using a syringe. A matrix solution containing 7 mg/ml NEDC in 70% MeOH (Cat. no. 34860; Sigma-Aldrich) was sprayed onto the tissue sections with the following instrumental parameters: nitrogen flow (5 psi), spray temperature ( $30^\circ\text{C}$ ), nozzle height (40 mm), 14 passes with offsets and rotations, and spray velocity (1200 mm/min), and isocratic flow of 60  $\mu\text{l}/\text{min}$  using 70% ACN as a pushing solvent.

### 2.4 | MALDI-MSI analysis

Mass spectrometry imaging analysis of tissue sections was performed on a timsTOF fleX instrument (Bruker Daltonics). The instrument was equipped with frequency tripled, 10 kHz, Nd:YAG laser (355 nm) (SmartBeam 3D; Bruker Daltonics). Imaging MS was collected at 10  $\mu\text{m}$  spatial resolution with beam scan off, using 200 laser shots per pixel. Data were collected in negative ion mode from  $m/z$  400–2000 Da. TIMS was performed in the range from  $1/K_0$  0.9 to  $1/K_0$  2.13  $\text{V}\cdot\text{s}/\text{cm}^2$  with a ramp time of 200 ms. External TOF calibration was performed with red phosphorous that was spotted next to the sections. TIMS was externally calibrated in electrospray ionization (ESI) mode using Tune Mix (Agilent). Single MS/MS spectra were acquired directly from tissue for some selected precursor ions at 50  $\mu\text{m}$  laser pitch. For that, the mass range was set from  $m/z$  50 to 1300 Da using a TIMS ramp from  $1/K_0$  0.5 to 1.7  $\text{V}\cdot\text{s}/\text{cm}^2$  with 200 ms ramp time. Six hundred laser shots were acquired per pixel in negative ion mode. Quadrupole isolation windows and collision energies were adapted for each precursor individually. If required, spectra from several pixels were accumulated, and collision energies were stepped from lower to higher voltages.

## 2.5 | Hyperspectral amyloid imaging

Amyloid pathology was further delineated using double staining with LCOs and hyperspectral confocal imaging. The LCOs quadroformyl thiophene acetic acid (qFTAA) and heptamer-formyl thiophene acetic acid (hFTAA) were used for staining polymorphic plaques (Nystrom et al., 2013). Following MALDI analysis, tissues were rinsed in absolute EtOH for 60 s, fixed in absolute EtOH (Cat no.: V002075; Sigma-Aldrich) at  $-20^{\circ}\text{C}$  for 8 min, 70% EtOH at  $-20^{\circ}\text{C}$  for 30 s, 70% EtOH at RT for 30 s, and rinsed for 5 min in PBS (Cat. no.: P9416; Sigma-Aldrich) both prior and after staining. For fluorescent amyloid staining, tissues were incubated with qFTAA ( $3\ \mu\text{M}$  in PBS) and hFTAA ( $1.5\ \mu\text{M}$  in PBS) in a humidification chamber for 30 min at RT. Tissues were mounted with Prolong Gold antifade reagent (Thermo-Fisher Scientific) and dried for 2 h at RT. Hyperspectral imaging was performed on ELYRA PS.1/LSM 780 laser scanning microscopy equipped with a 32-Channel GaAsP spectral detector (Zeiss). The objective used was Plan-Apochromat  $20\times/0.8$  (WD = 0.55 mm),  $\infty/0.17$ . The excitation wavelength for LCOs was 457 nm. The emission spectra were acquired in the range of 405–750 nm as described before (Nystrom et al., 2013).

## 2.6 | MSI data processing and analysis

Imaging data were processed in MATLAB R2020b with Bioinformatics Toolbox 4.14, Signal Processing Toolbox 8.4, and Image Processing Toolbox 11.1 (MathWorks, Inc.) installed. Multivariate modeling was performed in SIMCA software (v.17.0; Sartorius Stedim Data Analytics AB—Umetrics). MALDI imaging raw data files were converted into the imzML format using SCiLS Lab (v.2021b, Bruker Daltonics) and imported into the MATLAB programming environment using the imzMLConverter by Race et al. (2012). Data were normalized to total ion count and, in addition, for multivariate modeling purposes, log-transformation was applied to address heteroscedasticity and skewness. Data were centered but not scaled for multivariate modeling. Spatial segmentation of MSI data sets was performed on score images from principal component analysis (PCA), whereby images with the most pronounced plaques or plaque core features, respectively, were used. Segmentation of plaque cores was achieved by thresholding pixel values followed by removal of off-plaque localizing pixels. Segmentation of plaque structures was achieved using Otsu's global threshold followed by a series refinement including image erosion, image dilation, active contours algorithm, and removal of off-plaque localizing pixels. Image segmentation was further guided by hyperspectral fluorescence microscopy data.

Hyperspectral imaging raw data files in czi format were imported into MATLAB using code obtained from [https://github.com/CamachoDejay/czi\\_spec\\_im\\_load](https://github.com/CamachoDejay/czi_spec_im_load) (CamachoDejay, czi\_spec\_im\_load, 2020, github, [https://github.com/CamachoDejay/czi\\_spec\\_im\\_load](https://github.com/CamachoDejay/czi_spec_im_load)) together with the Bio-Formats software tool (Linkert et al., 2010). Binary maps of each ROI were used to subset data sets by

logical indexing and averaging pixel values for statistical data analysis. Further, binary maps served as discriminator matrices for supervised multivariate analysis. Orthogonal projection to latent structure-discriminant analysis (OPLS-DA) was used to discriminate between ROIs such as plaques, plaque cores, and peripheral plaque regions. OPLS-DA is a regression method that has evolved from Partial Least Squares (PLS) where class membership is supplied in a discriminator matrix (Y-matrix) to decompose the systematic variation in the data set (X-matrix) into Y-correlated (predictive) and Y-uncorrelated (orthogonal) variation (Bylesjö et al., 2006). The separation between the predictive and orthogonal components facilitates the interpretation of the predictive loading vector and provides a direct measure of the influence each of the variables has on the model. The number of relevant components for the models was estimated through seven-block cross-validation (CV). Orthogonal components based on CV were reduced to further prevent the overfitting of the OPLS-DA models. The number of orthogonal components was then based on meaningful orthogonal variation pertaining to, for example, cores in OPLS-DA models for plaques versus nonplaque. Finally, the correlation-scaled loadings,  $p(\text{corr})$ , were examined in order to identify differences in the lipidomic profiles between areas of interest at both age groups. Post-hoc power analyses were performed in MATLAB using the *sampsizepwr* function (Statistics and Machine Learning Toolbox).

High-loading variables were further subjected to *t*-test statistics and evaluated on single-ion images. Post-hoc power analyses and *t* statistics were performed in Matlab using the *sampsizepwr* function (Statistics and Machine Learning Toolbox). Power analysis was based on a two-sample pooled *t* test, after assessing for normally distributed data, with unknown standard deviation and equal variances. Mean and standard deviation of sample values from image-segmented arrays were used. Although we acknowledge that the usefulness of post-hoc power analyses is controversial, we included these results as retrospective assessments to safeguard against experimental error.

Together this approach allowed for the identification of significantly altered species which were further interrogated by single-ion images based on both *m/z* and their collisional cross-section (CCS). For this, mass spectral and mobility information of the MALDI-TIMS imaging data were extracted using TIMS Data Viewer 1.0 (Bruker Daltonics) and visualized using SCiLS Lab 2021b.

## 2.7 | Lipid identification

### 2.7.1 | Lipid extraction and LC-TIMS analyses

Lipids were extracted according to a previously reported procedure with slight modifications (Marsching et al., 2014). Briefly, the tissue was homogenized for 2 min on ice in 2 ml methanol and 300  $\mu\text{l}$  water with an Ultra Turrax T25 basic (IKA Labortechnik) at 24,000 rpm in a 15 ml polypropylene vial. The homogenate was transferred into a glass vial and the polypropylene vial was rinsed two times with 500  $\mu\text{l}$  methanol. Afterward, 3 ml of chloroform (Cat. no. 650498; Sigma-Aldrich) were added to get a solvent mixture of chloroform/

methanol/water (10:10:1, v/v/v). The extract was centrifuged for 10 min at 1008 g, and the supernatant was collected in a separate glass vial. Extraction was completed by repetition of this procedure twice, one time with 3 ml chloroform/methanol/water (10:10:1, v/v/v) and the second time with a 30:60:8 (v/v/v) mixture. Every extraction step included 2 min of sonication. The pooled extracts were dried under a nitrogen stream (37°C). Finally, the extract was dissolved in 100 µl chloroform/methanol/water (10:10:1, v/v/v) per 100 mg brain wet weight and stored at -20°C.

For LC-MS an ultra-high-pressure chromatography system (Bruker Elute UHPLC) was used to separate lipids on a YMC Triart C18 column (100 × 2.1 mm, 1.9 µm), packed with 1.9 µm material. The column compartment was heated to 55°C, and lipids were separated with a binary gradient at a constant flow rate of 400 ml/min. Mobile phases A and B were ACN:H<sub>2</sub>O 60:40% (v/v) and IPA:ACN:H<sub>2</sub>O 90:8:2% (v/v), both buffered with 0.1% formic acid and 10 mM ammonium formate. The 20-min LC-MS experiment started by ramping the mobile phase B from 40% to 43% within 2 min, to 50% within 2.1 min, to 54% within 12 min, to 70% within 12.1 min, and finally 99% within 18 min. It was decreased to 40% within 18.1 min and kept there until 20 min to re-equilibrate the column. The injection volume was 5 µl.

The MS analysis was performed in negative-ion mode as previously described using the PASEF acquisition mode (Vasilopoulou et al., 2020). Briefly, the LC was coupled to a hybrid trapped ion mobility-quadrupole time-of-flight mass spectrometer (timsTOF Pro; Bruker Daltonics) via an Apollo II ESI ion source (Bruker Daltonics). The voltage capillary was set to 4200 V and the TIMS ion charge control to 7.5 Mio counts. The accumulation and ramp time was set to 100 ms. Mass spectra were recorded in a range of  $m/z$  100–1500, and the ion mobility was scanned from 0.55 to 1.90 V-s/cm<sup>2</sup>. Precursors for data-dependent acquisition were isolated within the entire  $m/z$  mass range and fragmented with a constant collision energy of 35 eV. If necessary, the precursors were automatically fragmented multiple times within the same run to increase the quality of their MS/MS spectra. The mass calibration was performed using a mixture of sodium formate clusters with Agilent ESI LC-MS Tune Mix (50:50). The TIMS dimension was calibrated linearly using the same mixture.

## 2.7.2 | Initial processing of LC-PASEF data

The raw data were processed with MetaboScape (v. 2021b, Bruker Daltonics) using a mass range of 100–1200  $m/z$  and a retention time range of 20 min. The feature finding algorithm T-ReX 4D automatically extracts all information in the four-dimensional space ( $m/z$ , retention time, ion mobility, and intensity) and assigns MS/MS spectra to the features. For detection, an intensity threshold of >500 counts in positive and negative ion modes was used. The  $m/z$  and mobility dimensions were calibrated in MetaboScape automatically. The minimum 4D peak size was set to 100 data points or 75 data points in three out of five replicates using recursive feature extraction. [M+H]<sup>+</sup> ions were used as primary ions with [M+Na]<sup>+</sup> and [M+NH<sub>4</sub>]<sup>+</sup> as seed ions in positive and [M-H]<sup>-</sup> as primary and [M+HCOO]<sup>-</sup> as seed ions in

negative ion mode. The positive and negative mode data were merged using a tolerance of 2 ppm for  $m/z$  and 6 s for retention times.

## 2.7.3 | Lipid annotation based on LC-PASEF data

The lipid annotations were performed on merged positive and negative mode data using a generic rule-based annotation tool implemented in MetaboScape. As a library-free approach, published fragmentation rules were applied to profile in total 42 lipid subclasses from four categories: glycerolipids (GL), glycerophospholipids (GP), sphingolipids (SP), and sterol lipids (SL). The precursor ion mass tolerance was set to 5 ppm, the isotopic pattern matching (mSigma) value to 250 (ranging from 0 = perfect match to 1000 = no match), and the MS/MS matching score to 450. The results were manually inspected and obvious false annotations were removed using a 4D Kendrick Mass Defect Plot analysis (plotting exact mass vs. KMD [H or CH<sub>2</sub>]), with a color coding used for retention times and the bubble sizes used to display CCS values. The generated lists of lipids were exported for further use.

## 2.7.4 | Annotation of lipids in MALDI images

Lipids were annotated in MetaboScape (v.2021b, Bruker Daltonics) following the extraction of the four-dimensional data ( $m/z$ , ion mobility, intensity, and spatial coordinate). Briefly, spectra of the entire measurement region per sample were exported from SCiLS Lab (v.2021c) and imported into MetaboScape (v.2021b). Spectra from 10 × 10 pixels were averaged before feature extraction using the T-Rex<sup>3</sup> processing algorithm. An intensity threshold of 200 was used for peak detection and [M-H]<sup>-</sup> ions were selected as a primary ion, seed ions were forbidden.

Features were then annotated using an analyte list of mouse brain lipids that were previously identified using LC-ESI-PASEF allowing a mass error of 5 ppm and a CCS value deviation of 3% if available.

For additional confidence, MALDI TIMS MS/MS fragment spectra from some selected precursors were analyzed with MetaboScape (v.2021b). Fragment spectra were converted to \*.mgf format and added to the corresponding entry in the existing feature table in MetaboScape. The lipid identification is based on comparisons against a spectral library or molecular formula generation based on exact mass and fragment prediction.

# 3 | RESULTS

## 3.1 | Integrated MALDI TIMS TOF MSI and fluorescent amyloid imaging for multivariate classification of plaque pathology

We here employed a multidimensional MSI strategy using a novel MALDI-trapped ion mobility spectrometry TOF instrument to delineate plaque pathology-associated lipid species with increased



identification confidence. This is achieved through the ion mobility dimension of the used instrument that expands the molecular coverage of the MSI analyses at reasonable analysis times and most importantly increases molecular specificity through additional molecular parameters, that is, mass accuracy and CCS. Using this advanced MSI approach, we investigated plaque-associated changes in lipid localization in transgenic AD mice (tgAPP<sup>Swe</sup>) from two perspectives, including amyloid plaque polymorphism and age. For this, we multiplexed the TIMS MSI analyses with complementary structure sensitive amyloid staining performed on the same section and followed plaque pathology and plaque polymorphism in tgAPP<sup>SWE</sup> mice at different ages (18 and 23 months).

In TIMS, additional data are generated across the ion mobility dimension for each mass window in addition to the  $m/z$  dimension leading

consequently to very large data file sizes. To approach these complex, highly dimensional data in an unbiased way, we performed multistage image data processing and image segmentation analysis (Figure 1).

Following data processing, we performed PCA of the data for image segmentation (Figures 1b and 2a,b). This allowed us to obtain PCA images containing plaque-specific single-ion information that we subsequently used for image segmentation. In detail, binary maps were generated for the classification of plaque structures into four regions of interest including (1) plaques and (2) background as well as (3) plaque core, and (4) plaque periphery. Binary maps were generated through a combination of thresholding and active contours segmentation to annotate the different ROI in an unbiased way across all single plaques within each tissue sample and mouse, respectively (Figure 2a–f).

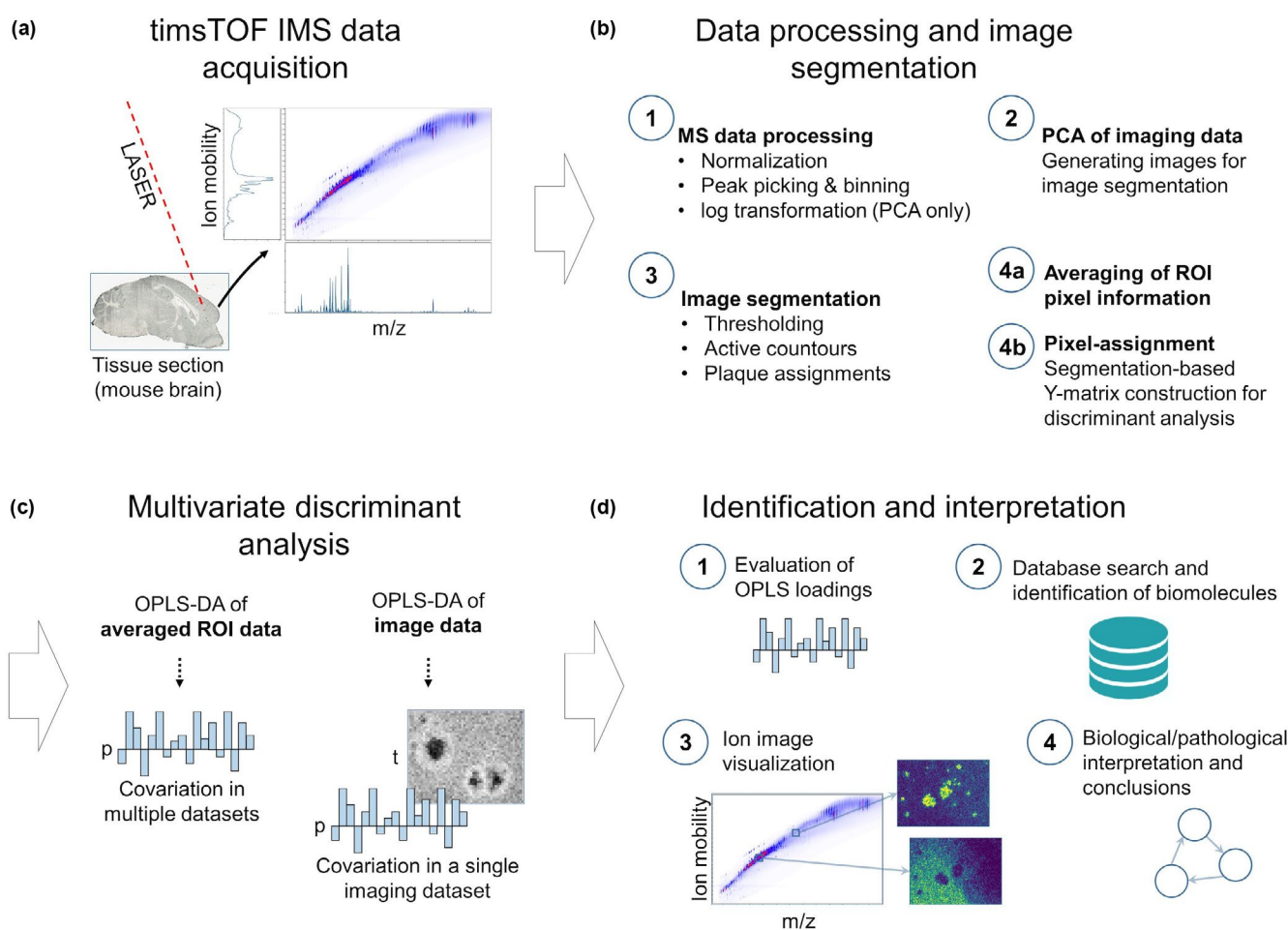


**FIGURE 1** Schematic workflow for processing and statistical analysis of TIMS TOF MSI data. TIMS TOF MSI data were acquired on (a) cortical areas of transgenic AD mouse models (tgAPP<sup>Swe</sup>), (b) imaging raw data were processed, and PCA was performed in order to generate (scores) images for image segmentation. Image segmentation was performed by a combination of thresholding and active contours segmentation. Segmented image areas were either averaged for statistical analysis or were used to construct a Y-matrix for discriminant analysis. (c) OPLS-DA was performed on averaged ROI data or imaging data to examine analytes that drive class separation. (d) Results of OPLS-DA were evaluated, the identities of important loadings were determined by database search (MetaboScape), and ion images were visualized for interpretation. AD, Alzheimer's disease; LCO, luminescent-conjugated oligothiophenes; MSI, mass spectrometry imaging; OPLS-DA, orthogonal projection to latent structure-discriminant analysis; PCA, principal component analysis; ROI, region of interest; TIMS, trapped ion mobility spectrometry; TOF, time of flight

### 3.2 | Hyperspectral microscopy with TIMS MSI reveals chemostructural heterogeneity within A $\beta$ plaques

Alzheimer's disease pathology is highly heterogeneous, involving most prominently polymorphic amyloid deposits including senile, cored plaques, as well as diffuse plaques (Masters et al., 2015; Scheltens et al., 2016). In clinical diagnosis, a binary assessment of highly aggregated amyloid assemblies is typically performed using congo red (CR) or thioflavin. The advent of a new class of amyloid probes, LCO, offer conformation-specific detection of polymorphic amyloid structures, which revealed age-dependent changes in conformational amyloid polymorphism within individual plaques, conformation-specific properties of prions, and, most recently, variability in A $\beta$  aggregate structures between plaques of AD subtypes (e.g., fAD, sAD) (Klingstedt et al., 2013; Magnusson et al., 2014; Nystrom et al., 2013; Rasmussen et al., 2017). Most importantly, our lab demonstrated the integration of these probes with MSI, allowing multimodal chemical and structural imaging of structurally distinct plaques (Michno et al., 2018).

In this study, we therefore multiplexed TIMS MSI with differential LCO staining for hyperspectral imaging of polymorphic A $\beta$  at the single plaque level. Following MSI acquisition, we performed LCO double staining using q-FTAA and h-FTAA on the same tissue sections (Figure 2g). Both probes have different emission properties, allowing hyperspectral delineation of differential LCO binding (Figure 2h). Here, q-FTAA staining was chosen to allow visualization of highly aggregated, mature fibrillary structures within A $\beta$  plaques, while in contrast, immature, protofibrillar A $\beta$  intermediates were visualized through preferential h-FTAA binding as illustrated by cross-sectional emission profiles (Figure 2i) (Klingstedt et al., 2013; Nystrom et al., 2013). The two fluorophores were imaged together using a hyperspectral setup, allowing subsequent image segmentation into more and less-aggregated A $\beta$  using linear unmixing-based image analysis (Figure 2j-l).

The MSI binary maps generated through PCA were then aligned with the linearly unmixed LCO data (Figure 2m-o; Figures S1 and S2). Here, the heterogeneity in the hyperspectral imaging data, that contained highly aggregated, q-FTAA-dominant features (purple), and less-aggregated forms of A $\beta$  fibrils that were h-FTAA dominant (green) (Figure 2j-l), were used as guidance for class assignment of subsequent orthogonal projection to latent structures-discriminant analysis (OPLS-DA). MSI pixel data within the generated ROI and that were corresponding between both imaging modalities were selected for subsequent statistical data analysis.

Together, this allowed for annotation and validation of both amyloid-positive features in general (plaque vs. background) as well as plaque structural diversity based on the conformational state of the amyloid- $\beta$  aggregates that predominate within a single plaque (core vs. periphery, Figure 2m-o).

Following ROI annotation and classification, the MSI pixel data were either averaged for statistical analysis or were used to construct a Y-matrix for discriminant analysis. OPLS-DA was used to

discriminate between regions of interest both within and between data sets (Figure 3). Here the aim was to interrogate the lipid localization diversity accounting for differences between plaque versus background and between plaque cores and peripheries of individual plaques, respectively, and finally for differences between plaques and plaque regions of animals of 18 and 23 months of age.

For this, the data were analyzed through two independent approaches. First, the data were interrogated in a Y2 matrix, where either plaque versus background or periphery versus core of the plaques was analyzed across all animals both for 18- and 23-month-old animals (Figure 3e,f,k,l; Figure S3). This analysis allowed for the extraction of key features separating the respective groups for all animals within a given age group. A limitation of this approach is the lack of possibility to visualize the unique features responsible for the separation of the fine plaque subcomponents in the context of a single animal. Therefore, we performed a second round of analysis that was based on a Y3-matrix. This approach allowed for the extraction of unique features that underlie the separation of background from plaque cores and periphery within individual animals. Here, for the features that allow classification into the respective region of interest (ROI; i.e., plaque, core, periphery), no major difference was observed between the different age groups and between the different animals, confirming the validity of the first analysis based on averaged ROI data.

This approach, however, did allow to visualize the distribution of the subgroup separating components in the form of component ion images (Figure 3a,b,g,h). The generated score images further validated the accurate ROI annotation and classification procedure and were well in line with the OPLS-DA results obtained for the averaged pixel data that were used for groupwise comparisons.

Following OPLS-DA model generation and validation, interrogation of the OPLS-DA results allowed us then to examine which analytes drive the class separation of the different ROI, within individual plaques, and between plaques in respective data sets and ages. These significant OPLS loadings (variables) were further confirmed through univariate statistics and validated by inspecting their mobility resolved single-ion localization patterns (Figures 4 and 5; Figure S4).

Inspection of the multidimensional MSI data showed plaque ROI-associated mass peak localizations with overlapping isobaric lipid species as resolved by TIMS. Here, we made use of the additional separation dimension, trapped ion mobility, which allows us to visualize isobaric or isomeric compounds (Figures 4 and 5). Peak separation of isobaric can in theory also be achieved with high resolving power instrumentations such as FTMS. However, acquisition at these mass resolutions requires long scan times of about 2–3 s/mass spectrum. The TIMS MSI setup allows fully resolving those peaks at much shorter scan times allowing for MSI experiments to be conducted at 10% of the time.

Further, TIMS MSI provides another layer of molecular identification by providing analyte-specific CCS data along with the accurate mass. For our analysis, we made use of this feature for the identification of lipid features that were significantly different in the OPLS-DA and univariate analysis. The *m/z*/CCS data obtained for

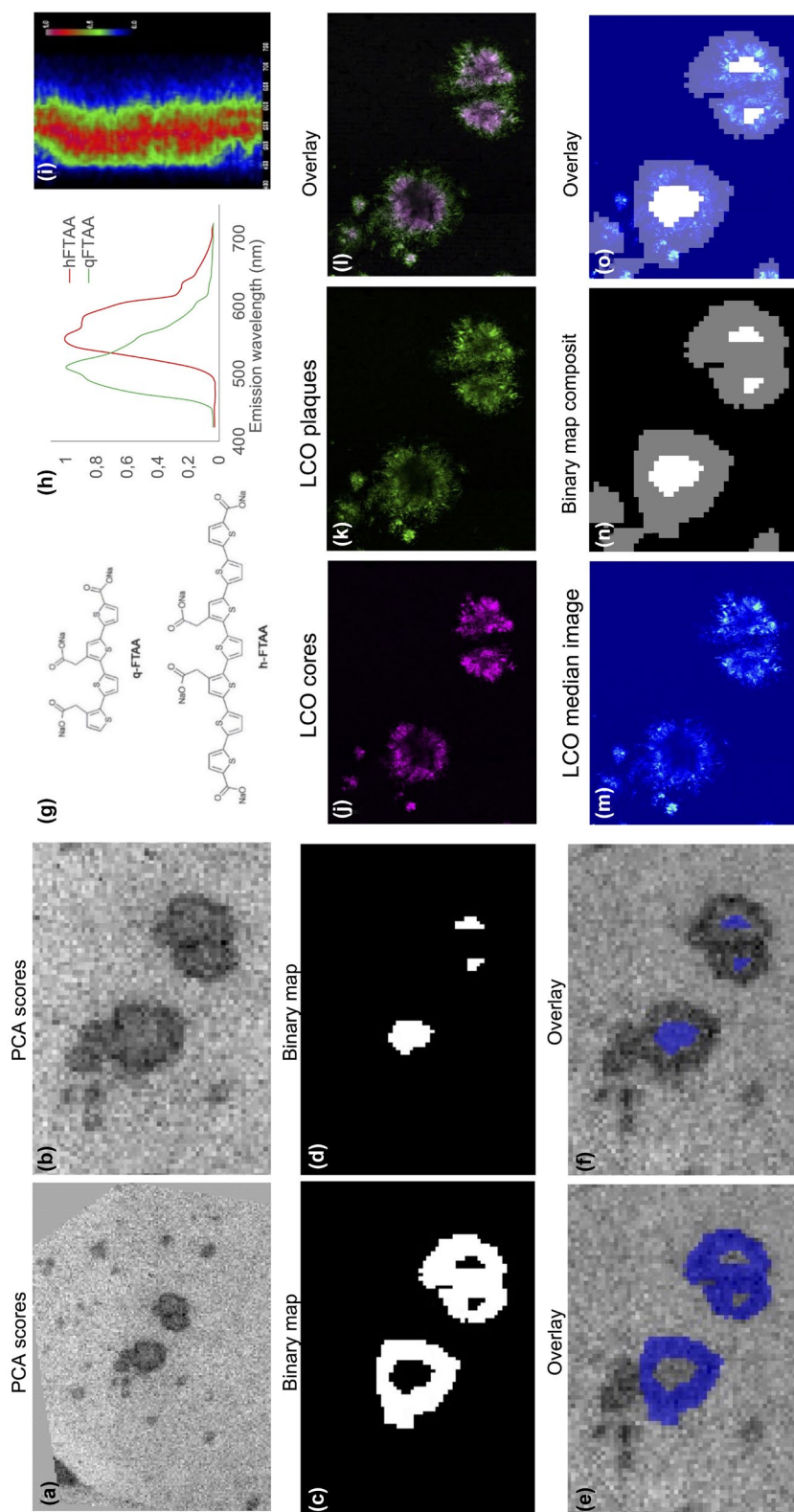


**FIGURE 2** Multivariate image segmentation using MSI and hyperspectral microscopy. Image segmentation for the pixel assignment was performed (a, b -zoom) on PCA scores image based on MSI data sets to generate (c, d -zoom) binary maps. This allowed for unbiased identification of A $\beta$  plaques (e) peripheries and (f) cores. Amyloid cross  $\beta$ -sheet conformation-specific LCOs, including (g) q-FTAA and h-FTAA, were used for identification of more (q-FTAA) and less (h-FTAA) aggregated A $\beta$  fibrils among A $\beta$  plaques. Here, the (h) emission profiles of these fluorophores were verified through heat map-based hyperspectral analysis of cross-sectional emission profiles of individual deposits (i). The LCO assigned plaque (j) cores, and (k) peripheries allowed for further binary characterization of the A $\beta$  plaques. For this purpose, the (m) LCO median spectral profiles were integrated with (n) MSI-based segmentation maps for an (o) efficient plaque structural diversity interrogation. LCO, luminescent-conjugated oligothiophenes; MSI, mass spectrometry imaging; PCA, principal component analysis



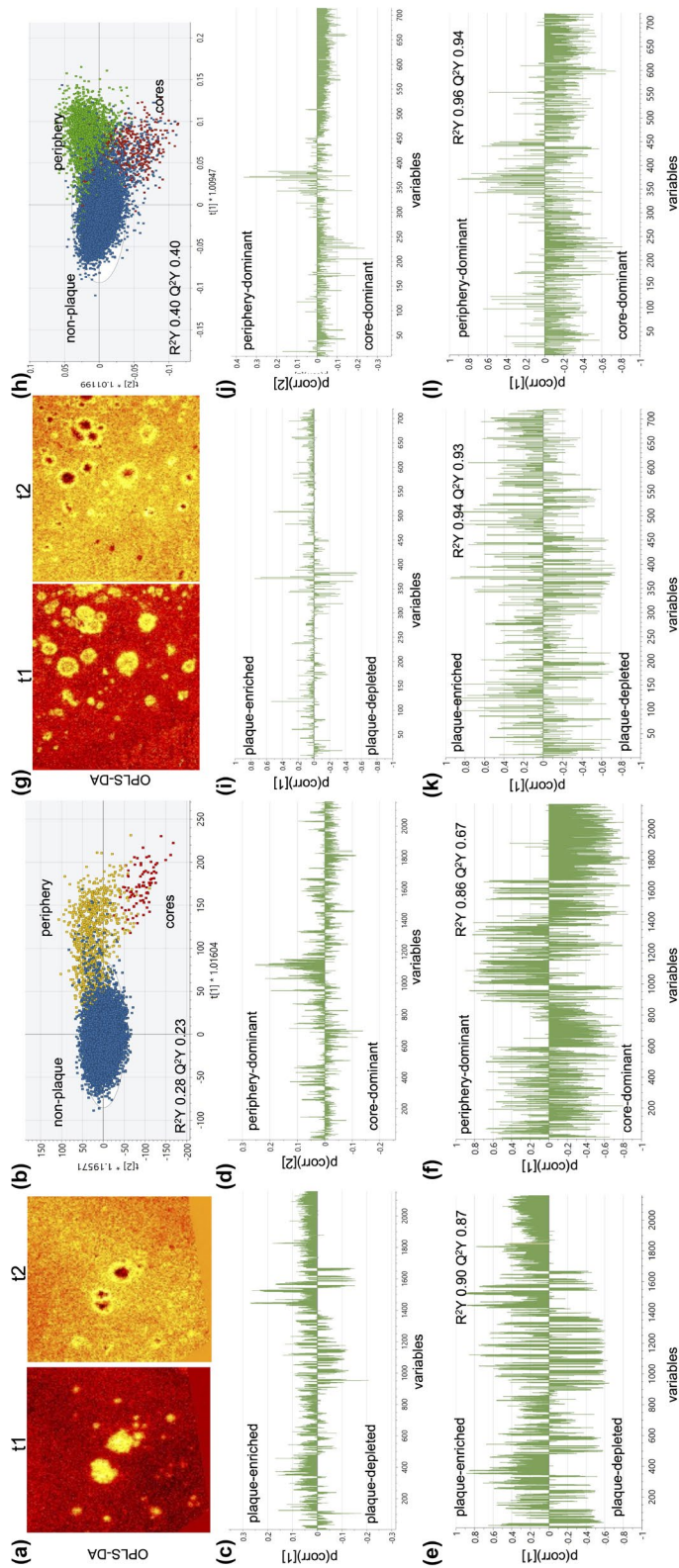


**FIGURE 3** OPLS-DA modeling of timsTOF MSI data on a single image basis and of plaque-averaged data. OPLS-DA on image basis for age groups 18 months (a–d) along with plaque-averaged data (number of animals  $n = 3$ , e, f). Similarly, OPLS on image data was performed for 23-month-old mice (number of animals  $n = 3$ , g–l). (a, g) Score images and corresponding (b, h) scatter plots as well as (c, d, i, j) loading plots for both the predictive components deduced from image-based OPLS-DA. (e, f, k, l) OPLS-DA modeling of plaque-averaged TMSI data: (e) 18 months, plaque versus nonplaque, (f) 18 months, periphery versus core, (k) 23 months, periphery versus core. MSI, mass spectrometry imaging; OPLS-DA, orthogonal projection to latent structure-discriminant analysis; TMSI, trapped ion mobility spectrometry; TOF, time of flight

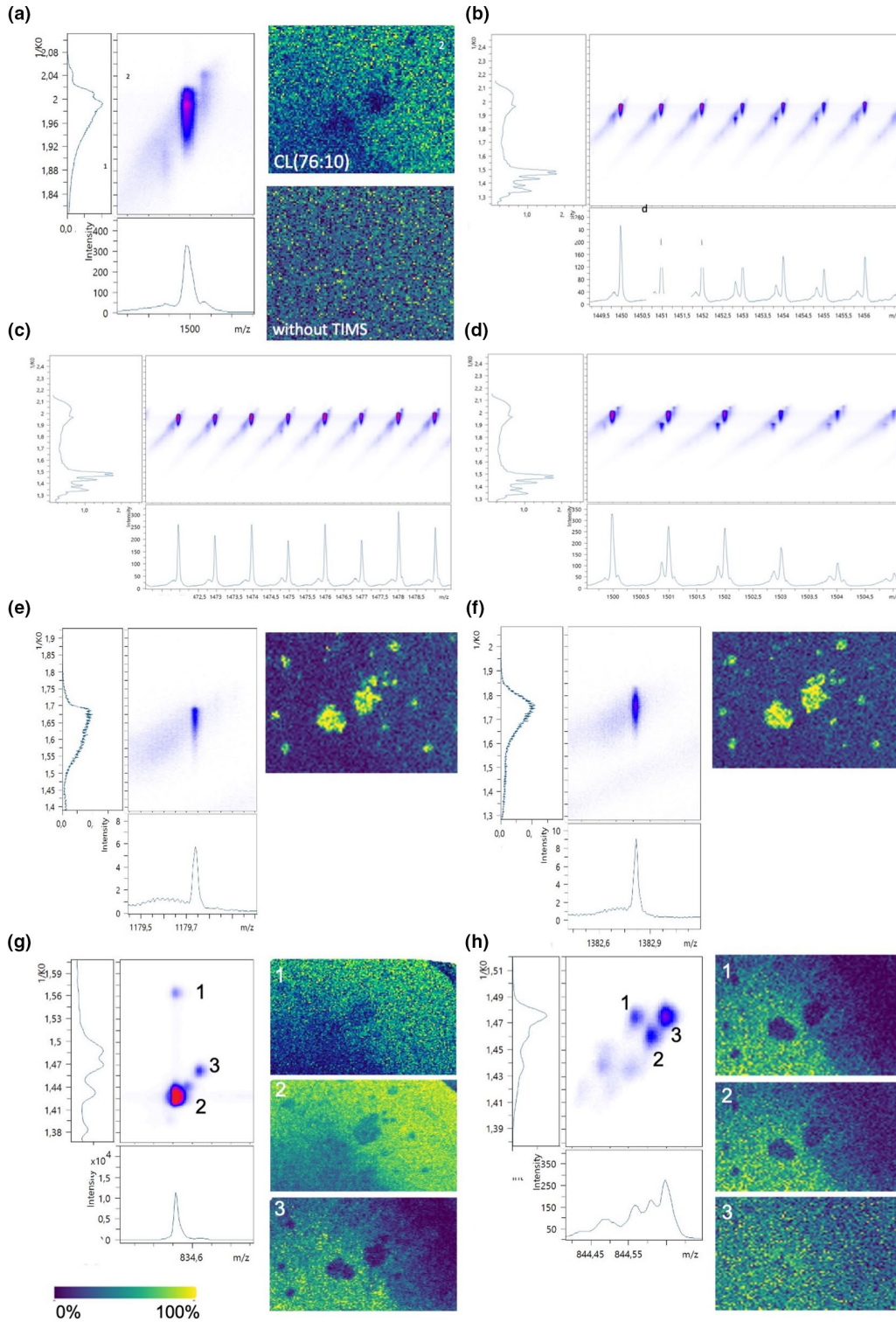


**FIGURE 4** Plaque-associated lipid patterns. Extraction of collision cross-sections of higher mass range ( $m/z$  1400–2000) from the trapped ion mobility mass spectrometry imaging allows for annotation of distinct cardiolipin (CL) ( $1499.996 \pm 0.05$   $1/K_0$   $1.987 \pm 0.02$   $V\cdot s/cm^2$ ) were specifically depleted within  $A\beta$  plaques. This trend was prominent for multiple CL species in between (b)  $m/z$  1449–1459, (c)  $m/z$  1469–1479, and (d)  $m/z$  1499–1509. Shorter mono-sialated gangliosides (GMs), including (e) GM3 (d36:1) ( $m/z$  1179.728  $1/K_0$  1.686  $V\cdot s/cm^2$ ) and (f) GM2 (d36:1) ( $m/z$  1382.818  $1/K_0$  1.750  $V\cdot s/cm^2$ ) did also display a general  $A\beta$  plaque trend with localization to these  $A\beta$  inclusions. These species were well resolved without the need for TIMS dimensionality. Finally, TIMS MSI allowed for identification of  $A\beta$  plaque-associated depletion patterns of phosphatidylserine (PS) species that otherwise partly overlapped with phosphatidylethanolamine (PE) species. These included (g) 1. PS (18:0/22:6) ( $m/z$  834.525  $1/K_0$  1.431  $V\cdot s/cm^2$ ), 2. PE (22:6/22:6) ( $m/z$  834.51  $1/K_0$  1.564  $V\cdot s/cm^2$ ), 3. ST (d18:1/20:0) ( $m/z$  834.5771  $1/K_0$  1.461  $V\cdot s/cm^2$ ), and (h) 1. PE (22:6/22:1) ( $m/z$  844.586  $1/K_0$  1.475  $V\cdot s/cm^2$ ), 2. PS (22:0/18:1) ( $m/z$  844.607  $1/K_0$  1.461  $V\cdot s/cm^2$ ), 3. unassigned. Number of animals  $n = 3$ . MSI, mass spectrometry imaging; TIMS, trapped ion mobility spectrometry



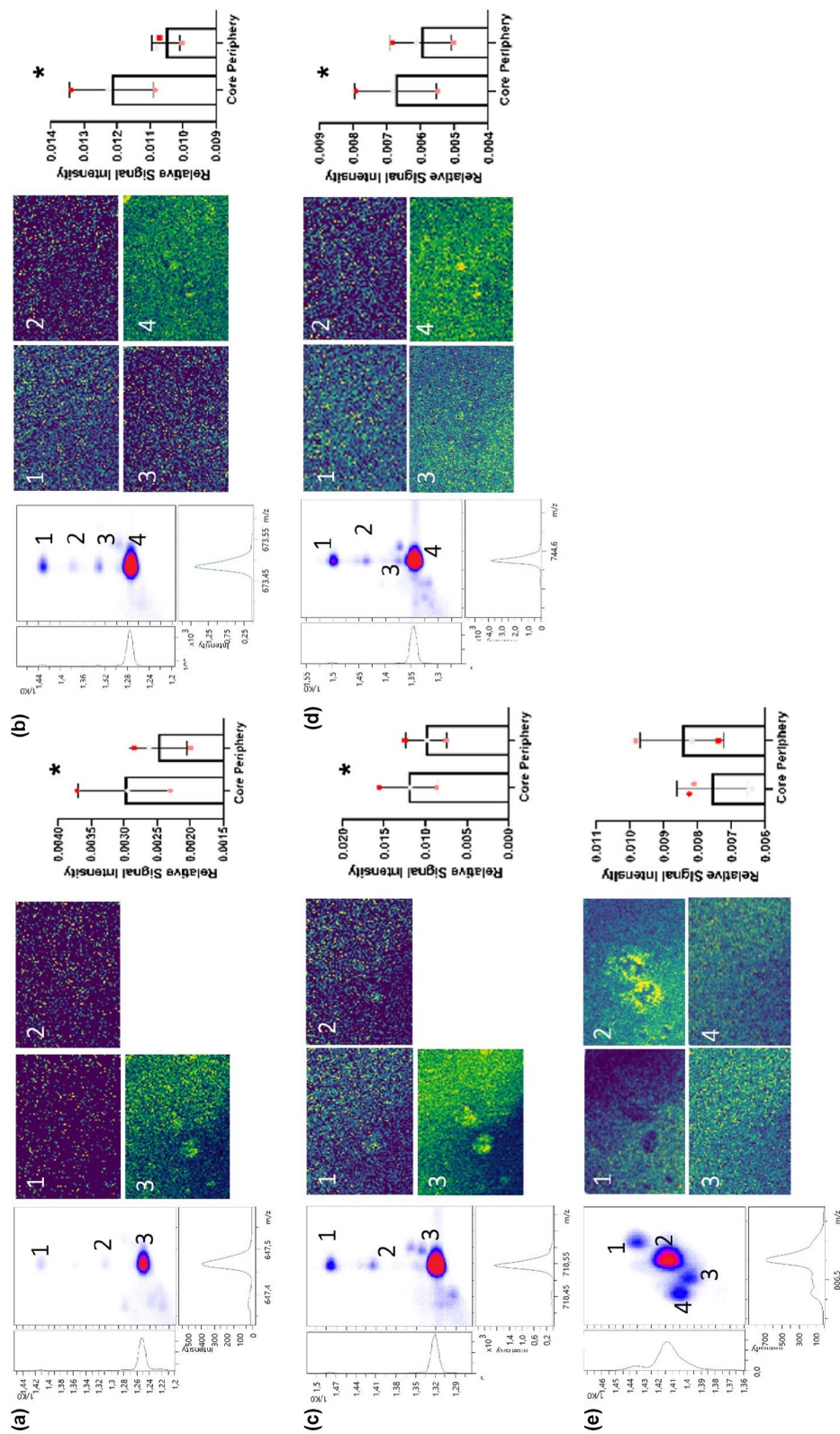


**FIGURE 5** Trapped ion mobility mass spectrometry imaging allows for extraction of distinct morphologic features associated with Aβ plaque cores. Here, ion mobility mass spectrometry imaging allowed for identification of core-specific localization phosphatidic acids (PA), including (a) PA (16:0/16:0) (*m/z* 647.464  $1/K_0$  1.221 *V-s/cm*<sup>2</sup>) and (b) PA (16:0/18:1) (*m/z* 673.479  $1/K_0$  1.244 *V-s/cm*<sup>2</sup>). Further, a similar localization was observed for phosphatidyl-ethanolamine species (PE), including (c) PE (34:0) (*m/z* 718.534  $1/K_0$  1.289 *V-s/cm*<sup>2</sup>), (d) PE (18:1/18:0) (*m/z* 744.554  $1/K_0$  1.315 *V-s/cm*<sup>2</sup>). Interestingly, trapped ion mobility mass spectrometry imaging allowed for identification of plaque-specific depletion of a phosphatidylserine species, (e) 1. PS (16:0/22:6) (*m/z* 806.501  $1/K_0$  1.404 *V-s/cm*<sup>2</sup>), and a unique localization of another lipid species putatively assigned as 2. ST (d36:1) (*m/z* 806.546  $1/K_0$  1.415 *V-s/cm*<sup>2</sup>). We verified the identity and side chain composition of both the PAs and the ST (d36:1) species using on tissue MS/MS analysis (Figures S5 and S6). Data indicate mean  $\pm$  SD, number of animals *n* = 3, *N* = 5–10 plaques. \* *p*  $\leq$  0.05, paired ratio *t*-test

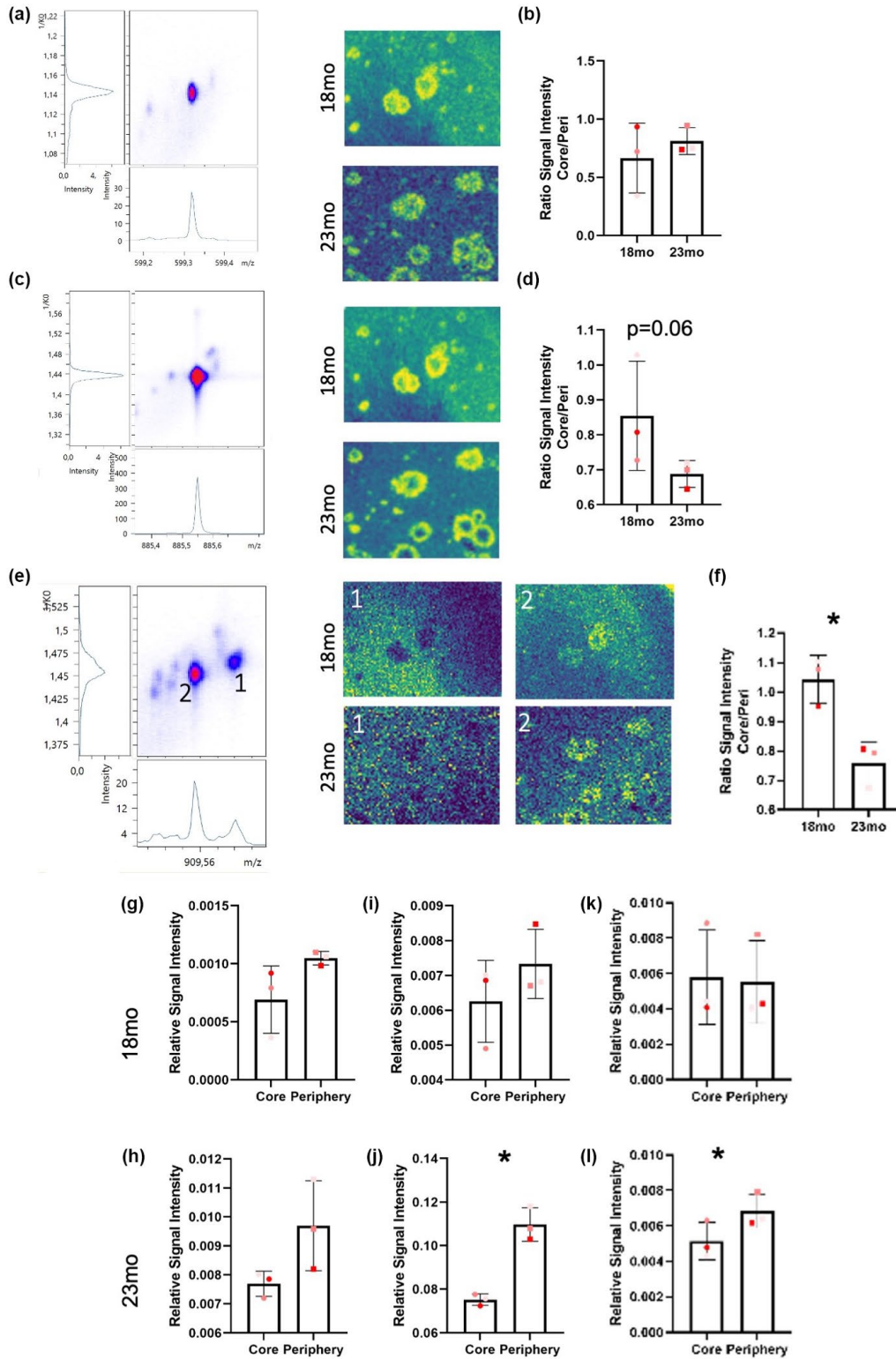


**FIGURE 6** TIMS imaging allows for the identification of distinct phosphoinositol lipid changes associated with A $\beta$  plaque maturation. Lyso-phosphoinositol LPI (18:0) ( $m/z$  599.32  $1/K_0$  1.142  $V\cdot s/cm^2$ ) (a, b) and PI (18:0/20:4) ( $m/z$  885.54  $1/K_0$  1.440  $V\cdot s/cm^2$ ) did not display age-related changes in localization to A $\beta$  deposits (c, d), though PI (18:0/20:4) showed a trend ( $p = 0.06$ ) toward relative increase in plaque periphery in older animals. PI (18:0/22:6) (e.2) ( $m/z$  909.55  $1/K_0$  1.455  $V\cdot s/cm^2$ ) showed a relative increase in the periphery compared with a core of A $\beta$  plaques in 23-month-old animals compared with 18-month-old animals. This is illustrated by a decrease in the core/periphery signal ratio (d, f). Comparative statistics within each age group show relative higher peripheral localization of PI at 23 months but not 18 months for both PI (18:0/20:4) (i, j) and PI (18:0/22:6) (k, l), while no age differences were associated for LPI (18:0) (g, h), b, d, f: Data indicate mean  $\pm$  SD, number of animals  $n = 3$ /age,  $N = 5$ –10 plaques. \* $p \leq 0.05$ , Student's  $t$ -test. g–l: Data indicate mean  $\pm$  SD, number of animals  $n = 3$ /age,  $N = 5$ –10 plaques. \* $p \leq 0.05$ , paired ratio  $t$ -test





each statistically different lipid compound were further validated through the offline analysis of mouse brain tissue extracts using liquid chromatography coupled to ESI TIMS TOF MS/MS. The TIMS MSI data ( $m/z$ /CCS) were matched against a generated database consisting of both the  $m/z$ /CCS and MS/MS data obtained by the LC-ESI TIMS experiments (Table S1). Together, this approach generated a list of confidently identified lipid species that were statistically significant in between the different groups compared, including plaques versus background, plaque core and plaque periphery, as well as 18- and 23-month-old mice.

### 3.3 | TIMS resolves plaque-associated lipids beyond mass

Next, we proceeded to inspect the OPLS-DA-derived and -identified lipid species that underlie a general A $\beta$  plaque-associated localization pattern. Here, TIMS MSI allows for the generation of clean, single-ion images without any interfering compounds as there is no other signal visible in the heat map display. The results showed a depletion of multiple species in the higher mass range ( $m/z$  1400–2000). Investigation of the trapped ion mobility MSI allowed for the identification of distinct cardiolipins (CL) (Figure 4a–d). Further, a general plaque-associated localization of mono-sialated gangliosides (GM), including GM2 and GM3 species was also observed (Figure 4e–f). TIMS MSI further allowed for identifying plaque-associated depletion patterns of phosphatidylserine (PS) species, PS 40:6 and PS 40:1, that partly overlapped with phosphatidylethanolamine (PE) and sulfatide (ST) species (Figure 4g,h).

### 3.4 | Plaque polymorphism is associated with distinct lipid localization patterns

Investigation of the TIMS mobilograms underlying the core- and periphery-enriched components revealed core-specific localization of several phospholipid species, such as phosphatidic acids (PA), including PA (32:0) and PA (34:1) (Figure 5a,b). Validation through LC-MS/MS and in situ MALDI TIMS MS/MS identified the side chain composition for those PA species to be 16:0/16:0 and 16:0/18:1, respectively (Figure S5). The results further show a morphology-specific localization of PE. In particular, PE (34:0) and PE (36:1) were observed to localize to the A $\beta$  plaque cores (Figure 5c,d). Due to the TIMS capabilities, we were able to observe a unique colocalization of PS (16:0/22:6) and a second lipid species ( $m/z$  806.5) putatively assigned as sulfatide (ST), in particular ST (d36:1) (Figure 5e; Figure S6). We have previously reported the localization of the ST (d36:1) to the periphery and outside of the A $\beta$  plaques (Michno et al., 2018); however, definitive assignment of the ST species was not possible due to the presence of isobaric compounds. Here thanks to the CCS value, we were able to attribute the signal depletion at the plaque to PS (16:0/22:6) species and confidently annotate the specific localization toward

the plaque rim to ST (d36:1), as further by on-tissue MALDI TIMS MS/MS as ST (16:0/20:1) (Figure S6).

### 3.5 | Progressing plaque pathology is characterized by distinct lipid accumulation

Following these analyses, we proceeded to investigate age-related changes in plaque lipid microenvironment in 23 -months-old mice compared with 18-month-old animals. To assess changes in relative lipid localization, we compared plaque versus nonplaque tissue as well as core versus periphery within each group using OPLS-DA. Here, no differences were observed between plaque-associated and plaque-depleted lipid localization patterns when comparing the significant loading values of the models generated for 18 and 23 months, respectively. Similarly, no absolute differences of lipid changes were observed for polymorphism-related models, core versus periphery, generated for 18- and 23 -months-old animals, though differences in loading values for certain lipid species were detected. To further assess these relative changes between the two age groups, we then compared the ratio of the core/periphery signal across the ages. Here, we observed mainly changes in phosphatidylinositols (PI). In more detail, lyso-phosphatidylinositol, LPI (18:0), did not display any significant, age-related changes (Figure 6a,b), while the larger, arachidonic acid-conjugated PI (18:0/20:4) species showed a trend toward a decrease in the core/periphery signal ratio with age ( $p = 0.06$ ) (Figure 6c,d). This pattern was even more prominent for a previously unreported, docosahexaenoic acid-conjugated PI (18:0/22:6) (Figure 6e,f). This lipid showed a significant difference in relative localization in between the plaque regions with a relative increase in the periphery compared with the core in 23-month-old mice compared with this ratio in 18-month-old mice. The relative signal intensity of those inositol species in between core and periphery within the age groups showed that for all three species, a more pronounced relative localization to the periphery compared with the cores in the 23-month-old compared with the 18-month-old mice (Figure 6g–i).

## 4 | DISCUSSION

The molecular mechanisms underlying AD pathogenesis are still not fully understood. Lipids have been implicated to play a central role in AD pathogenesis. Indeed, a global alteration is observed in cerebrospinal fluid, blood, and brain tissue extracts from AD patients before (Di Paolo & Kim, 2011). Multiple studies have also demonstrated alterations of various lipids and lipid metabolites both between A $\beta$  plaque microenvironment and even within single A $\beta$  plaques making use of the unique capabilities of MSI (Kaya, Brinet, Michno, Baskurt, et al., 2017; Kaya, Brinet, Michno, Syvanen, et al., 2017; Kaya et al., 2018; Michno et al., 2018).

In the present study, we extended MSI based spatial lipid analysis of AD plaque pathology towards TIMS--MSI. We further



implemented this imaging modality with hyperspectral microscopy data based on conformation-sensitive amyloid probes acquired on the same tissues similar to a previous study performed in our lab (Michno et al., 2018). The novelty of the current study is the full integration of the multimodal imaging data in the multivariate data analysis workflow to identify and outline structurally different amyloid morphology within individual deposits and the associated lipid patterns, respectively.

On the general plaque level, TIMS MSI identified plaque-specific localization of gangliosides, while CL, phosphoserines, and sulfatides were found depleted at plaque regions. Previous MSI studies have found a general localization of GM2, and GM3 with C18:0 and C20:0 fatty acid (FA) moieties, to A $\beta$  plaques that are independent of A $\beta$  plaques morphology (Kaya et al., 2018; Michno et al., 2018). Previous non-MSI studies have also identified enrichment of GM2 and GM3 species in both human AD and AD mouse models (Chan et al., 2012; Pernber et al., 2012). A plaque pathology-associated increase in gangliosides is in line with previous data that show that glycolipids enriched lipid rafts interact with beta-amyloid and hence promote aggregation.

In contrast, a plaque-associated depletion of cardiolipin is most likely a consequence of neuronal degradation. Brain cardiolipin has previously been outlined with MSI (Amoscato et al., 2014) and CL is highly enriched in the inner membrane of mitochondria of nerve cells. CL depletion consequently indicates neuronal degradation presumably a result of oxidative stress affecting the mitochondria. Further in line with our data, impaired CL metabolism has been reported to be a consequence of amyloid pathology (Monteiro-Cardoso et al., 2015).

Along with the CL pattern, a plaque-associated depletion of poly-unsaturated FA-containing PE and PS lipids is observed. While this is in line with previously published results, indicating depletion of these species, these previous data were based solely on putative identification (Kaya et al., 2018; Michno et al., 2018). Our present study provides a clear separation and identification of these species facilitated through the ion mobility modality of TIMS MSI. The depletion of PUFA-containing phospholipids is well in line with previous studies that suggest PUFA-lipid degradation to be a result of lipid-peroxidation through amyloid pathology-induced oxidative stress (Butterfield & Lauderback, 2002).

The second part of our analysis comprised the delineation and identification of spatial lipid distributions associated with structural amyloid heterogeneity within individual deposits. For this, the TIMS MSI analyses were integrated with hyperspectral amyloid imaging followed by comprehensive data analysis using multivariate modeling. Here, the results revealed a distinct, plaque core-associated lipid pattern for PA and PE species.

PA is considered a key building block for phospholipid synthesis and also functions as a second messenger. Although debated, involvement of PA in AD has been suggested, partially due to the anionic nature of PA and hence its potential role as TREM2 ligand and partially due to suggested alterations in phospholipases D (PLD) in AD (Oliveira et al., 2010; Tanguy et al., 2019; Wang et al., 2015).

Specifically, some of the PLD isoforms have been shown to be responsible for PA synthesis from among other CL as well as phosphatidylcholine (PC) (Jang et al., 2012).

In addition to PA, some PE species showed characteristic distribution to the plaque core, which is in contrast to the depletion of DHA-containing PE species. PE is highly abundant in cholesterol-enriched detergent-resistant microdomains (DRM) of neuronal membranes. While the link of cholesterol and AD plaque pathology has been discussed for decades (Barrett et al., 2012; Chen et al., 2021; Di Paolo & Kim, 2011), PE has been directly linked to A $\beta$  pathology through modulation of membrane-associated proteins both  $\alpha$ -secretase and  $\gamma$ -secretase. Here, decreased PE levels were found to lead to reduced amyloidogenic processing of APP and reduced A $\beta$  generation, respectively (Area-Gomez et al., 2012; Nestic et al., 2012). Plaque-associated PE therefore indicates a PE-APP/A $\beta$  interaction, presumably of DRM-associated PE, that is aggravating A $\beta$  secretion and aggregation into mature deposits.

In addition to the core-specific localizations observed for PA and PE, a putatively assigned sulfatide, ST (d36:1), was found to be increased at the outer periphery of the plaque. The signal distribution of this ST species was different to the general, signal depletion pattern observed for other, larger ST species, associated with demyelination (Kaya et al., 2020). Here, TIMS MSI resolved this ST species from PS and identified this compound as ST (16:0/20:1). This unique localization of ST with the short FA might highlight the presence of unique cell populations, such as astrocytes (Isaac et al., 2006), yet again highlighting the potential of TIMS MSI for studies of A $\beta$  plaque molecular microenvironment.

Finally, we investigated relative changes in lipid localization associated with progressing plaque pathology in old mice at 23 months, which reflects very advanced and severe pathology and hence provides a good comparison point for these mice. The rationale of these analyses was that progressing plaque pathology with aging is associated with the accumulation of distinct lipids. Following OPLS-DA modeling of core periphery data with each age group yielded no difference with respect to the species that were different in between the plaque structures. This is in line with a previous study by our lab, where we followed amyloid peptide deposition over different ages of the tgSwe model (6, 9, 12, 18 and 23 months) (Michno et al., 2020). To assess relative changes in spatial lipid localization, we investigated the top-loadings using univariate comparison of their portioning ratio in between core and periphery across the two age groups.

Here, we observed relatively increased levels of PI (18:0/22:6) in the periphery compared with the core in plaques at higher age compared with the core/periphery ratio of this species at 18 months. We have previously reported a clear localization of PI and lyso-PI (LPI), including LPI (18:0) and PI (18:0/20:4), to the periphery of A $\beta$  deposits (Michno, Wehrli, et al., 2019; Michno et al., 2018). An increase of lipid localization, to intra-plaque structure heterogeneity as observed for PI (18:0, 22:6), might indicate plaque maturation. Interestingly, the here observed PI (18:0/22:6) exhibits a similar FA configuration as the secondary messenger,

phosphoinositolbiphosphate (PIP2). These PI species have been linked to progressing amyloid pathology, where a decrease in PIP2 along with an increase in corresponding PI was observed in the context A $\beta$  oligomerization (Arancio, 2008; Berman et al., 2008). A major observation though for the age comparisons was a rather static pattern of plaque morphology-associated lipid localizations with progressing plaque pathology at advanced age. This is in line with previous data on relative A $\beta$  peptide levels published by our lab (Michno et al., 2020), where plaque morphology-associated differences were more prominent rather than age-associated differences in plaque-associated A $\beta$  content. This suggests that most plaques have reached a plateau in A $\beta$  uptake, on plaque processing and plaque growth, respectively.

Based on our results, it is clear that in order to truly delineate spatial lipid dynamics, kinetic studies of lipid accumulation in A $\beta$  proximity might be needed. Indeed, such approaches have been previously utilized, for instance, to follow surfactant metabolism in the lung (Ellis et al., 2021). Further, our lab recently utilized such a kinetic approach, in an imaging stable isotope labeling kinetic study (iSILK), where we followed A $\beta$  peptide deposition during A $\beta$  plaque maturation (Michno et al., 2021).

## 5 | CONCLUSION

In summary, this work highlights the potential of in situ mapping and annotation of isobaric lipid species in the context of AD-specific A $\beta$  plaque pathology. This was achieved through combined MALDI-MSI coupled with trapped ion mobility separation and structural A $\beta$  conformational characterization through hyperspectral imaging. Using this approach, we were able to obtain well resolved single-ion patterns of multiple lipid classes (PS, PE, PA, GM, ST, CL, and PI) localizing to A $\beta$  plaque pathology and intra-plaque amyloid heterogeneity, respectively. We further show that progressing plaque pathology is associated with relatively increased localization of PI to diffuse plaque structures. Together, this multimodal imaging approach combining hyperspectral conformational analysis and multidimensional MSI is demonstrated to be a powerful approach for studying molecular microenvironments of histologically confined pathologic features such as A $\beta$  plaque pathology.

## ACKNOWLEDGEMENTS

We thank Dr. Stina Syvänen and Dr. Dag Sehlin at Uppsala University for providing the tgAPP<sup>Swe</sup> mouse brain samples. The work was in part performed at the imaging MS infrastructure at the University of Gothenburg. We thank Prof. Per Hammarström and Prof. Peter Nilsson at Linköping University for kindly providing the LCOs. We thank the staff at the Centre for Cellular Imaging (CCI), Core Facilities, The Sahlgrenska Academy, University of Gothenburg, for help with the development of the hyperspectral imaging paradigm and microscopy expertise. The Swedish Research Council VR (#2018-02181 JH, #2018-02532 HZ, and #2017-00915 KB), Alzheimerfonden (JH and KB), Alzheimer Research UK (JH), Hjärnfonden (HZ and KB), the

Knut and Alice Wallenberg Foundation (HZ and WM), the European Research Council (#681712 HZ), Swedish State Support for Clinical Research (#ALFGBG-720931 HZ), Åhlén-Stiftelsen (JH), Rune och Ulla Amlövs Stiftelse (PW), Stiftelsen Gamla Tjänarinnor (PW, JH, KB, and WM), Federal Ministry of Education and Research (BMBF; FH-Impuls Partnerschaft M2Aind; Project: M2OGA; Förderkennzeichen 13FH8I02IA; to CH), Gun och Bertil Stohnes Stiftelse (PW, JH, and WM), Agneta Prytz-Folkes och Gösta Folkes Stiftelse (PW), Torsten Söderberg Foundation (KB), Wilhelm & Martina Lundgrens Vetenskapsfond (PW), Demensfonden (JH, PW and WM), and Frimurarestiftelsen (HZ) are acknowledged for financial support.

All experiments were conducted in compliance with the ARRIVE guidelines.

## CONFLICT OF INTEREST

Sven W. Meyer, Janina Oetjen, and Corinna Henkel are employed at Bruker Daltonics GmbH & Co. KG, Bremen, Germany. Jörg Hanrieder is an editor for the Journal of Neurochemistry.

## AUTHOR CONTRIBUTIONS

JH conceived and designed the study. WM, JO, CM, SK, JG, KM, SM, and CHe performed experiments. PW designed and performed the multivariate statistical analyses. WM, PW, CM, SK, JG, SM, KM, KB, HZ, CHe, JO, Cho, and JH analyzed and discussed the data. WM, PW, CM, SM, JO, CHe, and JH wrote the manuscript.

## DATA AVAILABILITY STATEMENT

The data that support the findings of this study are available from the corresponding author upon reasonable request. A preprint of this article was posted on chemRxiv on October 19, 2021: <https://chemrxiv.org/engage/chemrxiv/article-details/616d32968b620d7399535eb6>.

## ORCID

Wojciech Michno  <https://orcid.org/0000-0002-3096-3604>

Henrik Zetterberg  <https://orcid.org/0000-0003-3930-4354>

Janina Oetjen  <https://orcid.org/0000-0002-4088-5742>

Carsten Hopf  <https://orcid.org/0000-0003-0802-6451>

Jörg Hanrieder  <https://orcid.org/0000-0001-6059-198X>

## REFERENCES

- Amoscato, A. A., Sparvero, L. J., He, R. R., Watkins, S., Bayir, H., & Kagan, V. E. (2014). Imaging mass spectrometry of diversified cardiolipin molecular species in the brain. *Analytical Chemistry*, 86, 6587–6595. <https://doi.org/10.1021/ac5011876>
- Arancio, O. (2008). PIP2: A new key player in Alzheimer's disease. *Cellscience*, 5, 44–47.
- Area-Gomez, E., del Carmen Lara Castillo, M., Tambini, M. D., Guardia-Laguarta, C., de Groof, A. J. C., Madra, M., Ikenouchi, J., Umeda, M., Bird, T. D., Sturley, S. L., & Schon, E. A. (2012). Upregulated function of mitochondria-associated ER membranes in Alzheimer disease. *EMBO Journal*, 31, 4106–4123. <https://doi.org/10.1038/emboj.2012.202>
- Barrett, P. J., Song, Y., Van Horn, W. D., Hustedt, E. J., Schafer, J. M., Hadziselimovic, A., Beel, A. J., & Sanders, C. R. (2012). The amyloid precursor protein has a flexible transmembrane domain and binds

- cholesterol. *Science*, 336, 1168–1171. <https://doi.org/10.1126/science.1219988>
- Berman, D. E., Dall'Armi, C., Voronov, S. V., McIntire, L. B. J., Zhang, H., Moore, A. Z., Staniszewski, A., Arancio, O., Kim, T.-W., & Di Paolo, G. (2008). Oligomeric amyloid- $\beta$  peptide disrupts phosphatidylinositol-4,5-bisphosphate metabolism. *Nature Neuroscience*, 11(5), 547–554. <https://doi.org/10.1038/nn.2100>
- Butterfield, D. A., & Lauderback, C. M. (2002). Lipid peroxidation and protein oxidation in Alzheimer's disease brain: Potential causes and consequences involving amyloid  $\beta$ -peptide-associated free radical oxidative stress. *Free Radical Biology and Medicine*, 32, 1050–1060.
- Bylesjö, M., Rantalainen, M., Cloarec, O., Nicholson, J. K., Holmes, E., & Trygg, J. (2006). OPLS discriminant analysis: Combining the strengths of PLS-DA and SIMCA classification. *Journal of Chemometrics*, 20, 341–351. <https://doi.org/10.1002/cem.1006>
- Chan, R. B., Oliveira, T. G., Cortes, E. P., Honig, L. S., Duff, K. E., Small, S. A., Wenk, M. R., Shui, G., & Di Paolo, G. (2012). Comparative lipidomic analysis of mouse and human brain with Alzheimer disease. *Journal of Biological Chemistry*, 287, 2678–2688.
- Chen, Y., Strickland, M. R., Soranno, A., & Holtzman, D. M. (2021). Apolipoprotein E: Structural insights and links to Alzheimer disease pathogenesis. *Neuron*, 109, 205–221. <https://doi.org/10.1016/j.neuron.2020.10.008>
- Di Paolo, G., & Kim, T.-W. (2011). Linking lipids to Alzheimer's disease: Cholesterol and beyond. *Nature Reviews Neuroscience*, 12(5), 284–296. <https://doi.org/10.1038/nrn3012>
- Ellis, S. R., Hall, E., Panchal, M., Flinders, B., Madsen, J., Koster, G., Heeren, R. M. A., Clark, H. W., & Postle, A. D. (2021). Mass spectrometry imaging of phosphatidylcholine metabolism in lungs administered with therapeutic surfactants and isotopic tracers. *Journal of Lipid Research*, 62, 100023.
- Enzlein, T., Cordes, J., Munteanu, B., Michno, W., Serneels, L., Strooper, B., De, H. J., Wolf, I., Chávez-Gutiérrez, L., & Hopf, C. (2020). Computational analysis of Alzheimer amyloid plaque composition in 2D- and elastically reconstructed 3D-MALDI MS images. *Analytical Chemistry*, 92(21), 14484–14493. <https://doi.org/10.1021/acs.analchem.0c02585>
- Gillig, K. J., Ruotolo, B., Stone, E. G., Russell, D. H., Fuhrer, K., Gonin, M., & Schultz, A. J. (2000). Coupling high-pressure MALDI with ion mobility/orthogonal time-of-flight mass spectrometry. *Analytical Chemistry*, 72, 3965–3971. <https://doi.org/10.1021/ac0005619>
- Hanrieder, J., Phan, N. T. N., Kurczyk, M. E., & Ewing, A. G. (2013). Imaging mass spectrometry in neuroscience. *ACS Chemical Neuroscience*, 4(5), 666–679. <https://doi.org/10.1021/cn400053c>
- Isaac, G., Pernber, Z., Gieselmann, V., Hansson, E., Bergquist, J., & Månsson, J.-E. (2006). Sulfatide with short fatty acid dominates in astrocytes and neurons. *FEBS Journal*, 273, 1782–1790. <https://doi.org/10.1111/j.1742-4658.2006.05195.x>
- Jackson, S. N., Ugarov, M., Egan, T., Post, J. D., Langlais, D., Albert, S. J., & Woods, A. S. (2007). MALDI-ion mobility-TOFMS imaging of lipids in rat brain tissue. *Journal of Mass Spectrometry*, 42, 1093–1098. <https://doi.org/10.1002/jms.1245>
- Jackson, S. N., Wang, H. Y., Woods, A. S., Ugarov, M., Egan, T., & Schultz, J. A. (2005). Direct tissue analysis of phospholipids in rat brain using MALDI-TOFMS and MALDI-ion mobility-TOFMS. *Journal of the American Society for Mass Spectrometry*, 16, 133–138. <https://doi.org/10.1016/j.jasms.2004.10.002>
- Jang, J.-H., Lee, C. S., Hwang, D., & Ryu, S. H. (2012). Understanding of the roles of phospholipase D and phosphatidic acid through their binding partners. *Progress in Lipid Research*, 51, 71–81. <https://doi.org/10.1016/j.plipres.2011.12.003>
- Kaya, I., Brinet, D., Michno, W., Baskurt, M., Zetterberg, H., Blenow, K., & Hanrieder, J. (2017). Novel trimodal MALDI imaging mass spectrometry (IMS3) at 10  $\mu$ m reveals spatial lipid and peptide correlates implicated in A $\beta$  plaque pathology in Alzheimer's disease. *ACS Chemical Neuroscience*, 8, 2778–2790.
- Kaya, I., Brinet, D., Michno, W., Syvanen, S., Sehlin, D., Zetterberg, H., Blenow, K., & Hanrieder, J. (2017). Delineating amyloid plaque associated neuronal sphingolipids in transgenic Alzheimer's disease mice (tgArcSwe) using MALDI imaging mass spectrometry. *ACS Chemical Neuroscience*, 8, 347–355. <https://doi.org/10.1021/acscchemneuro.6b00391>
- Kaya, I., Jennische, E., Lange, S., Tarik Baykal, A., Malmberg, P., & Fletcher, J. S. (2020). Brain region-specific amyloid plaque-associated myelin lipid loss, APOE deposition and disruption of the myelin sheath in familial Alzheimer's disease mice. *Journal of Neurochemistry*, 154, 84–98. <https://doi.org/10.1111/jnc.14999>
- Kaya, I., Zetterberg, H., Blenow, K., & Hanrieder, J. (2018). Shedding light on the molecular pathology of amyloid plaques in transgenic Alzheimer's disease mice using multimodal MALDI imaging mass spectrometry. *ACS Chemical Neuroscience*, 9(7), 1802–1817. <https://doi.org/10.1021/acscchemneuro.8b00121>
- Klingstedt, T., Shirani, H., Aslund, K. O., Cairns, N. J., Sigurdson, C. J., Goedert, M., & Nilsson, K. P. (2013). The structural basis for optimal performance of oligothiophene-based fluorescent amyloid ligands: Conformational flexibility is essential for spectral assignment of a diversity of protein aggregates. *Chemistry—A European Journal*, 19, 10179–10192. <https://doi.org/10.1002/chem.201301463>
- Linkert, M., Rueden, C. T., Allan, C., Burel, J.-M., Moore, W., Patterson, A., Loranger, B., Moore, J., Neves, C., MacDonald, D., Tarkowska, A., Sticco, C., Hill, E., Rossner, M., Eliceiri, K. W., & Swedlow, J. R. (2010). Metadata matters: Access to image data in the real world. *Journal of Cell Biology*, 189, 777–782. <https://doi.org/10.1083/jcb.201004104>
- Liu, C.-C., Kanekiyo, T., Xu, H., & Bu, G. (2013). Apolipoprotein E and Alzheimer disease: Risk, mechanisms and therapy. *Nature Reviews Neurology*, 9, 106–118. <https://doi.org/10.1038/nrnneurol.2012.263>
- Magnusson, K., Simon, R., Sjölander, D., Sigurdson, C. J., Hammarström, P., & Nilsson, K. P. R. (2014). Multimodal fluorescence microscopy of prion strain specific PrP deposits stained by thiophene-based amyloid ligands. *Prion*, 8, 319–329. <https://doi.org/10.4161/pri.29239>
- Marsching, C., Jennemann, R., Heilig, R., Gröne, H.-J., Hopf, C., & Sandhoff, R. (2014). Quantitative imaging mass spectrometry of renal sulfatides: Validation by classical mass spectrometric methods. *Journal of Lipid Research*, 55, 2343–2353. <https://doi.org/10.1194/jlr.M051821>
- Masters, C. L., Bateman, R., Blenow, K., Rowe, C. C., Sperling, R. A., & Cummings, J. L. (2015). Alzheimer's disease. *Nature Reviews Disease Primers*, 1(1). <https://doi.org/10.1038/nrdp.2015.56>
- McLean, J. A., Ridenour, W. B., & Caprioli, R. M. (2007). Profiling and imaging of tissues by imaging ion mobility-mass spectrometry. *Journal of Mass Spectrometry*, 42, 1099–1105. <https://doi.org/10.1002/jms.1254>
- Michno, W., Kaya, I., Nyström, S., Guerard, L., Nilsson, K. P. R., Hammarström, P., Blenow, K., Zetterberg, H., & Hanrieder, J. (2018). Multimodal chemical imaging of amyloid plaque polymorphism reveals A $\beta$  aggregation dependent anionic lipid accumulations and metabolism. *Analytical Chemistry*, 90(13), 8130–8138. <https://doi.org/10.1021/acs.analchem.8b01361>
- Michno, W., Nyström, S., Wehrli, P., Lashley, T., Brinkmalm, G., Guerard, L., Syvänen, S., Sehlin, D., Kaya, I., Brinet, D., Nilsson, K. P. R., Hammarström, P., Blenow, K., Zetterberg, H., & Hanrieder, J. (2019). Pyroglutamation of amyloid- $\beta$ -42 (A $\beta$ x-42) followed by A $\beta$ 1–40 deposition underlies plaque polymorphism in progressing Alzheimer's disease pathology. *Journal of Biological Chemistry*, 294(17), 6719–6732. <https://doi.org/10.1074/jbc.ra118.006604>
- Michno, W., Stringer, K. M., Enzlein, T., Passarelli, M. K., Escrig, S., Vitanova, K., Wood, J., Blenow, K., Zetterberg, H., Meibom, A., Hopf, C., Edwards, F. A., & Hanrieder, J. (2021). Following spatial A $\beta$  aggregation dynamics in evolving Alzheimer's disease pathology by imaging stable isotope labeling kinetics. *Science Advances*, 7, eabg4855. <https://doi.org/10.1126/sciadv.abg4855>





- Michno, W., Wehrli, P., Meier, S. R., Sehlin, D., Syvänen, S., Zetterberg, H., Blennow, K., & Hanrieder, J. (2020). Chemical imaging of evolving amyloid plaque pathology and associated A $\beta$  peptide aggregation in a transgenic mouse model of Alzheimer's disease. *Journal of Neurochemistry*, 152, 602–616. <https://doi.org/10.1111/jnc.14888>
- Michno, W., Wehrli, P. M., Zetterberg, H., Blennow, K., & Hanrieder, J. (2019). GM1 locates to mature amyloid structures implicating a prominent role for glycolipid-protein interactions in Alzheimer pathology. *Biochimica et Biophysica Acta (BBA)—Proteins and Proteomics*, 1867, 458–467. <https://doi.org/10.1016/j.bbapap.2018.09.010>
- Monteiro-Cardoso, V. F., Oliveira, M. M., Melo, T., Domingues, M. R. M., Moreira, P. I., Ferreira, E., Peixoto, F., & Videira, R. A. (2014). Cardiolipin profile changes are associated to the early synaptic mitochondrial dysfunction in Alzheimer's disease. *Journal of Alzheimer's Disease*, 43(4), 1375–1392. <https://doi.org/10.3233/jad-141002>
- Nesic, I., Guix, F. X., Vennekens, K., Michaki, V., Veldhoven, P. P., Van Veldhoven, P. P., De Strooper, B., Dotti, C. G., & Wahle, T. (2012). Alterations in phosphatidylethanolamine levels affect the generation of A $\beta$ . *Aging Cell*, 11, 63–72. <https://doi.org/10.1111/j.1474-9726.2011.00760.x>
- Nilsson, K. P. (2009). Small organic probes as amyloid specific ligands—past and recent molecular scaffolds. *FEBS Letters*, 583, 2593–2599. <https://doi.org/10.1016/j.febslet.2009.04.016>
- Nilsson, K. P. R., Åslund, A., Berg, I., Nyström, S., Konradsson, P., Herland, A., Inganäs, O., Stabo-Eeg, F., Lindgren, M., Westermark, G. T., Lannfelt, L., Nilsson, L. N. G., & Hammarström, P. (2007). Imaging distinct conformational states of amyloid- $\beta$  fibrils in Alzheimer's disease using novel luminescent probes. *ACS Chemical Biology*, 2(8), 553–560. <https://doi.org/10.1021/cb700116u>
- Nyström, S., Psonka-Antonczyk, K. M., Ellingsen, P. G., Johansson, L. B. G., Reitan, N., Handrick, S., Prokop, S., Heppner, F. L., Wegenast-Braun, B. M., Jucker, M., Lindgren, M., Stokke, B. T., Hammarström, P., & Nilsson, K. P. R. (2013). Evidence for age-dependent in vivo conformational rearrangement within A $\beta$  amyloid deposits. *ACS Chemical Biology*, 8(6), 1128–1133. <https://doi.org/10.1021/cb4000376>
- Oliveira, T. G., Chan, R. B., Tian, H., Laredo, M., Shui, G., Staniszewski, A., Zhang, H., Wang, L., Kim, T.-W., Duff, K. E., Wenk, M. R., Arancio, O., & Di Paolo, G. (2010). Phospholipase D2 ablation ameliorates Alzheimer's disease-linked synaptic dysfunction and cognitive deficits. *Journal of Neuroscience*, 30(49), 16419–16428. <https://doi.org/10.1523/JNEUROSCI.3317-10.2010>
- Pernber, Z., Blennow, K., Bogdanovic, N., Mansson, J. E., & Blomqvist, M. (2012). Altered distribution of the gangliosides GM1 and GM2 in Alzheimer's disease. *Dementia and Geriatric Cognitive Disorders*, 33, 174–188. <https://doi.org/10.1159/000338181>
- Philipson, O., Lord, A., Gumucio, A., O'Callaghan, P., Lannfelt, L., & Nilsson, L. N. G. (2010). Animal models of amyloid- $\beta$ -related pathologies in Alzheimer's disease. *FEBS Journal*, 277(6), 1389–1409. <https://doi.org/10.1111/j.1742-4658.2010.07564.x>
- Race, A. M., Styles, I. B., & Bunch, J. (2012). Inclusive sharing of mass spectrometry imaging data requires a converter for all. *Journal of Proteomics*, 75, 5111–5112. <https://doi.org/10.1016/j.jprot.2012.05.035>
- Rasmussen, J., Mahler, J., Beschoner, N., Kaeser, S. A., Häslar, L. M., Baumann, F., Nyström, S., Portelius, E., Blennow, K., Lashley, T., Fox, N. C., Sepulveda-Falla, D., Glatzel, M., Oblak, A. L., Ghetti, B., Nilsson, K. P. R., Hammarström, P., Staufenbiel, M., Walker, L. C., & Jucker, M. (2017). Amyloid polymorphisms constitute distinct clouds of conformational variants in different etiological subtypes of Alzheimer's disease. *Proceedings of the National Academy of Sciences of the United States of America*, 114, 13018–13023. <https://doi.org/10.1073/pnas.1713215114>
- Scheltens, P., Blennow, K., Breteler, M. M. B., de Strooper, B., Frisoni, G. B., Salloway, S., & Van der Flier, W. M. (2016). Alzheimer's disease. *The Lancet*, 388(10043), 505–517. [https://doi.org/10.1016/s0140-6736\(15\)01124-1](https://doi.org/10.1016/s0140-6736(15)01124-1)
- Tanguy, E., Wang, Q., Moine, H., & Vitale, N. (2019). Phosphatidic acid: From pleiotropic functions to neuronal pathology. *Frontiers in Cellular Neuroscience*, 13. <https://doi.org/10.3389/fncel.2019.00002>
- Trim, P. J., Henson, C. M., Avery, J. L., McEwen, A., Snel, M. F., Claude, E., Marshall, P. S., West, A., Princivalle, A. P., & Clench, M. R. (2008). Matrix-assisted laser desorption/ionization-ion mobility separation-mass spectrometry imaging of vinblastine in whole body tissue sections. *Analytical Chemistry*, 80, 8628–8634. <https://doi.org/10.1021/ac8015467>
- Vasilopoulou, C. G., Sulek, K., Brunner, A.-D., Meitei, N. S., Schweiger-Hufnagel, U., Meyer, S. W., Barsch, A., Mann, M., & Meier, F. (2020). Trapped ion mobility spectrometry and PASEF enable in-depth lipidomics from minimal sample amounts. *Nature Communications*, 11, 331.
- Wang, Y., Cella, M., Mallinson, K., Ulrich, J. D., Young, K. L., Robinette, M. L., Gilfillan, S., Krishnan, G. M., Sudhakar, S., Zinselmeier, B. H., Holtzman, D. M., Cirrito, J. R., & Colonna, M. (2015). TREM2 lipid sensing sustains the microglial response in an Alzheimer's disease model. *Cell*, 160, 1061–1071. <https://doi.org/10.1016/j.cell.2015.01.049>

## SUPPORTING INFORMATION

Additional supporting information may be found in the online version of the article at the publisher's website.

**How to cite this article:** Michno, W., Wehrli, P. M., Koutarapu, S., Marsching, C., Minta, K., Ge, J., Meyer, S. W., Zetterberg, H., Blennow, K., Henkel, C., Oetjen, J., Hopf, C., & Hanrieder, J. (2021). Structural amyloid plaque polymorphism is associated with distinct lipid accumulations revealed by trapped ion mobility mass spectrometry imaging. *Journal of Neurochemistry*, 00, 1–17. <https://doi.org/10.1111/jnc.15557>